Journal of Applied Polymer Science

Effects of the short-fiber tip geometry and interphase properties on the interfacial debonding behavior of rubber matrix composites

Xiaoming Yu, Boqin Gu, Bin Zhang
School of Mechanical and Power Engineering, Nanjing Tech University, Nanjing, People's Republic of China
Correspondence to: B. Gu (E-mail: bqgu@njtech.edu.cn)

ABSTRACT: An axisymmetric finite element model of a single fiber embedded in a rubber matrix was established. A cohesive zone model was used for the fiber–matrix interface because of the interfacial failure. The effect of the fiber tip shape on the interfacial debonding of short-fiber-reinforced rubber matrix sealing composites (SFRCs) was investigated; the shapes were flat, semi-elliptical, hemispherical, and conoid, respectively. The initial strain of the interfacial debonding (ε_0) was obtained. We found that among the researched fiber tips, ε_0 of the SFRC reinforced with the hemispherical tip fiber appeared to be the maximum. The initial locations of interfacial debonding were also determined. The results show that the initial locations of the interfacial debonding moved from the edge to the center of the fiber tip when the ratio of the semimajor axis and semiminor axis of the semi-elliptical fiber tip increased gradually. Further study on the effect of the interphase properties on ε_0 with the hemispherical fiber tip was conducted. The results indicate that an interphase thickness of 0.2 μm and an interphase elastic modulus of about 752 MPa were optimal for restraining the initiation of the interfacial debonding. © 2015 Wiley Periodicals, Inc. J. Appl. Polym. Sci. **2015**, *132*, 42774.

KEYWORDS: composites; fibers; rubber; surfaces and interfaces; theory and modeling

Received 16 March 2015; accepted 25 July 2015
DOI: 10.1002/app.42774

INTRODUCTION

Short-fiber-reinforced rubber matrix sealing composites (SFRCs), such as aramid-, glass-, and carbon-fiber-reinforced rubber sheets, are widely used in the petroleum, chemical, electrical, and mechanical industries. Fibers or particles embedded in a rubber matrix can effectively improve the comprehensive performance of materials, for example, the strength, fatigue resistance, corrosion resistance, compressibility, and resilience. Engineering practice has confirmed that these kinds of composites have had good applicability over recent years.[1,2]

A precise estimate of the initiation and evolution of the failure behavior is necessary to improve the reliability of composite utilization. Many investigations of the failure behavior of composite materials have been conducted. Zhang *et al.*[3] studied the effect of interfacial debonding on the failure behavior of short-fiber-reinforced rubber composites. Vaughan and McCarthy[4] pointed out that both the matrix and interphase properties affect the failure characteristics of composites. Hobbiebrunken *et al.*[5] and Canal *et al.*[6] presented experimental evidence of the interfacial debonding in composite failure by *in situ* observation. It is, therefore, clear that the failure behavior of composite materials is dependent upon many contributing factors, including their constituent properties and interfacial properties. The performances of composites, such as fiber-reinforced resin matrixes and metal matrixes, can be accurately predicted by mesoscopic numerical models.[7,8] However, rubber matrix composites have mechanical behavior that is more complicated because of special performances of the rubber (e.g., small modulus, large deformation, hyperelasticity), which lead to relatively rare research results.[9,10]

On the basis of the shear lag model, the self-consistent theory and equivalent inclusion theory, certain progress has been made in research on the influence of fiber mesoscopic parameters on the macroperformance of composites. However, there are too many simplifications and approximations in the existing theoretical analysis models, and the predictable results do not agree well with the experimental results. A finite element method based on real fiber geometry is an effective way to study such issues at a mesoscopic level. Nishikawa *et al.*[11] analyzed the fracture properties of the fiber–matrix interface in composites with fragmentation experiments. Simulation results based on the cohesive zone model compared well with the experimental data. Okabe *et al.*[12] predicted the number of fiber breaks during the single-fiber composite experiment. The results show that the results predicted by the numerical simulation agreed well with those measured by the experimental data.

Two-phase materials have been exploited for decades in engineering design, and they have great applicability and high performance. However, it has been suggested that some materials

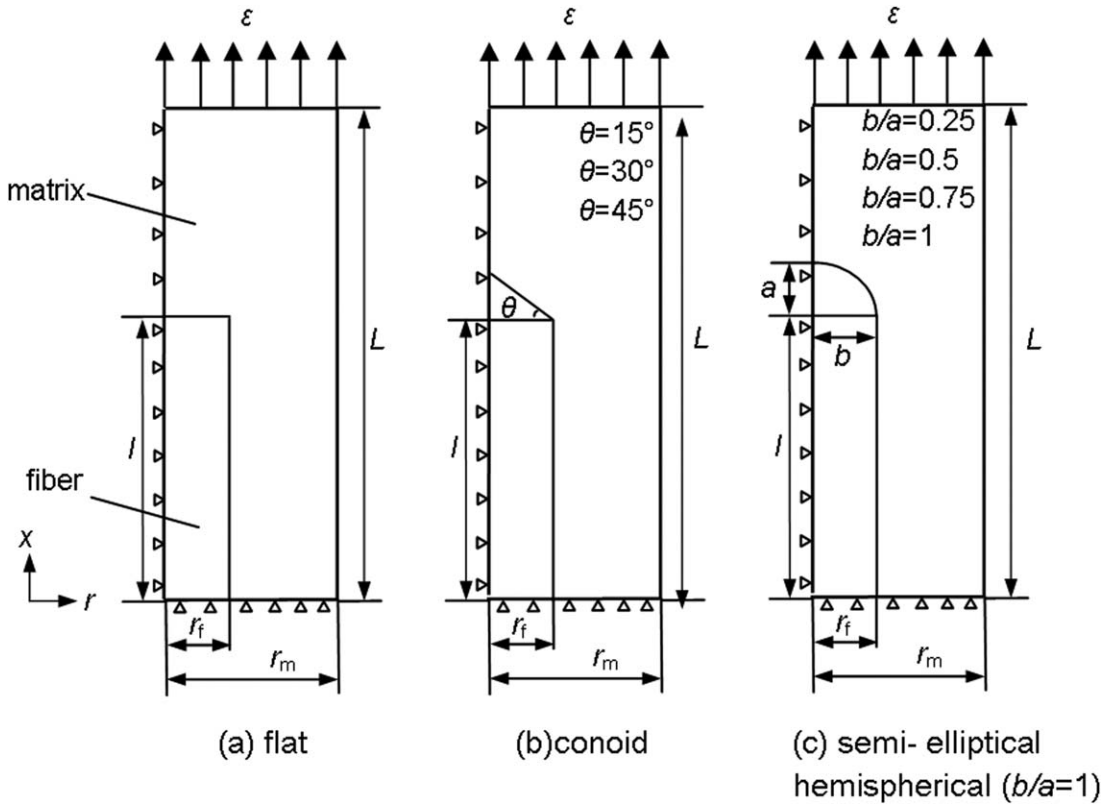

Figure 1. Shape and dimension of the fiber tip.

previously considered to be two-phase composites are better described in terms of a third phase, the interphase.[13–15] The interphase performance is considered a key factor in the study of the comprehensive mechanical performances of composites. Zhang and Gu[16] studied the effects of the interphase thickness (t) and elastic modulus on the properties of short-fiber-reinforced composite materials. Yuan *et al.*[17] established a finite element model (FEM) model of the interfacial reaction layer and analyzed the influence of the interphase reaction on the interphase shear strength of composites.

Although the interphase typically accounts for less than 2% of the total mass of the material in composites, it has been shown that the longitudinal tensile strength is improved by as much as 29%, the compressive strength is improved by as much as 50% and the notched fatigue lifetime cycles is improved by as many as two orders of magnitude.[18]

An interphase region can be on the order of 0.2 μm. However, definitive verification of t is usually impossible.[19] Kim *et al.*[20] measured t in a glass–epoxy composite by means of three different experimental techniques, namely, nanoindentation, nanoscratching, and differential scanning calorimetry tests, respectively. The results show three different values of t for the same material. Shen and Li[21] presented a selection of the interphase properties of short-fiber-reinforced composites. In many studies,[22–24] the performances of the interphase were not constants but varied with the thickness of the interphase.

Considerable work has been done on this subject in our previous work. We studied the effects of the short-fiber tip geometry and the inhomogeneous interphase on the stress distribution in SFRC.[25] This article is an extension of a previous work to investigate the effects of the fiber tip geometry and interphase properties on the interfacial debonding of SFRCs. An FEM under an axial tensile load was established, where a cohesive zone model was embedded in the fiber–matrix interface. In the modeling strategy, the initial strain of the interfacial debonding (ε_0) of the interfacial debonding with different short-fiber tip shapes are discussed, and the optimum shape of the fiber tip is determined. Furthermore, the effects of t and the modulus on the interfacial debonding of SFRCs were investigated.

COMPUTATIONAL MICROMECHANICS MODEL

Generation of the Representative Volume Element

An FEM was created with the package ABAQUS/Standard (2010). To investigate the effect of the fiber tip shapes on the interfacial debonding behavior of the SFRCs, four kinds of fiber tip shapes were taken into consideration, and they were flat, conoid, hemispherical, and semi-elliptical, respectively, as shown in Figure 1. We assumed that the fiber had a constant fiber radius (r_f) of 7.5 μm[26] and a ratio of the fiber length (l) to the diameter (l/r_f) of 5. The matrix had a constant matrix radius ($r_m = 5r_f$) and half-length ($L = 2l$). The angle (θ) of the conoid fiber tip is shown in Figure 1(b). a and b are the semimajor axis and semiminor axis of the semi-elliptical fiber tip, respectively, as shown in Figure 1(c). The physical model was assumed to consist of a fiber surrounded by the matrix and subjected to a uniform tension load parallel to the fiber direction. Only one-quarter of the actual physical model

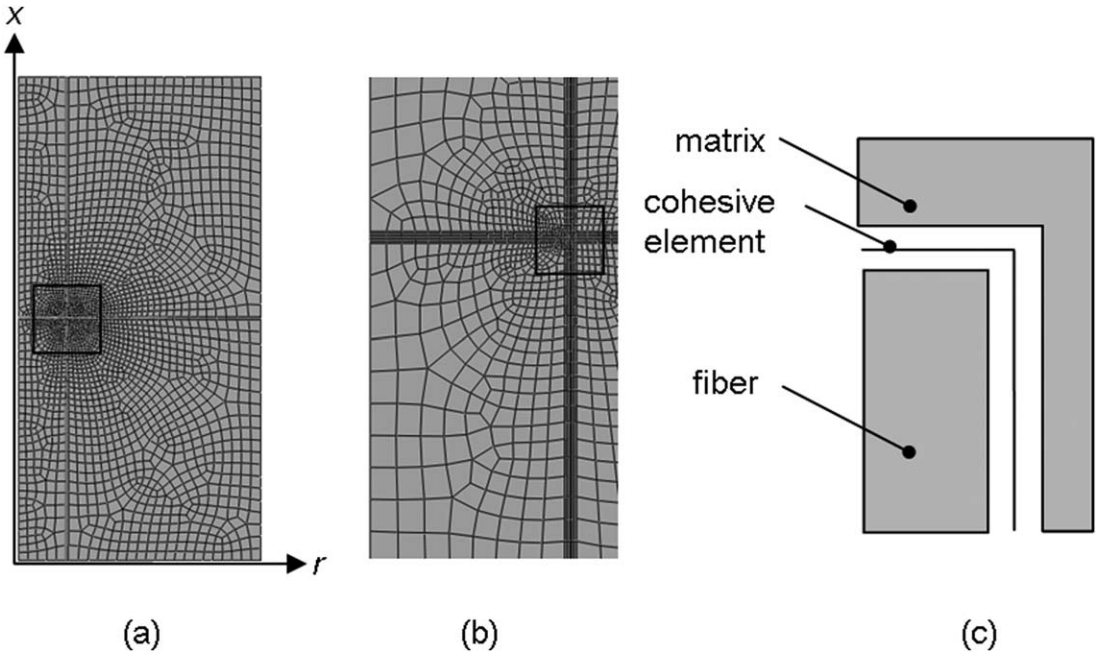

Figure 2. Finite element meshes: (a) whole model for calculation, (b) partially enlarged, and (c) individual constituents.

was required in the analysis because of the axisymmetric symmetry.

For this FEM, the boundary conditions included:

$$\begin{aligned} u_r &= 0 \quad \text{at } r = 0 \\ u_x &= 0 \quad \text{at } x = 0 \\ u_x &= U \quad \text{at } x = L \end{aligned} \tag{1}$$

where u_r and u_x are the displacements in the r and x directions, respectively, and U is the displacement at $x = L$. The strain (ε) is equal to U/L, and the boundary of the model at $r = r_m$ is enforced to hold straight during deformation.

A detailed finite element mesh of a typical flat fiber tip is shown in Figure 2, where the grid is refined at the edge of fiber tip. The mesh in the regions where high material degradation or high stress concentration was expected to occur was refined. The four-node quadrilateral axisymmetric element was used in the model. Two different sets of elements were used to model the fiber and matrix, respectively. The fiber was modeled with the linear elastic element CAX4, namely, a four-node bilinear quadrilateral axisymmetric element. The matrix was modeled as a hyperelastic purely incompressible material; this required the use of elements with a

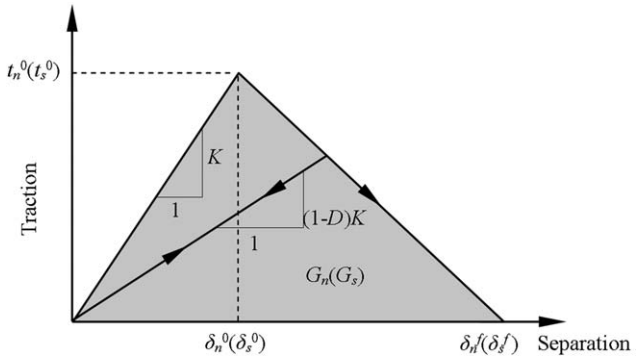

Figure 3. Traction–separation law of the cohesive element.

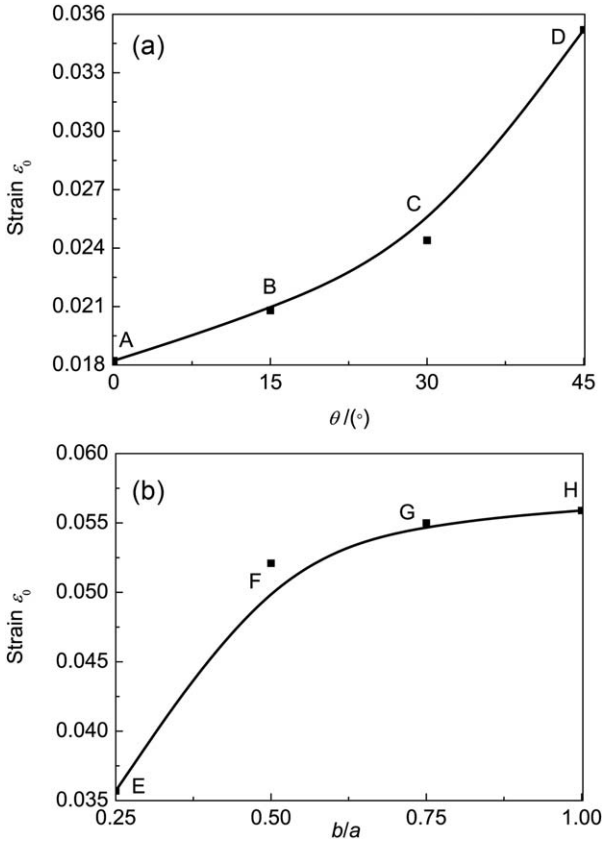

Figure 4. ε_0 values of the (a) flat and conoid short-fiber tips and (b) semi-elliptical and hemispherical short-fiber tips.

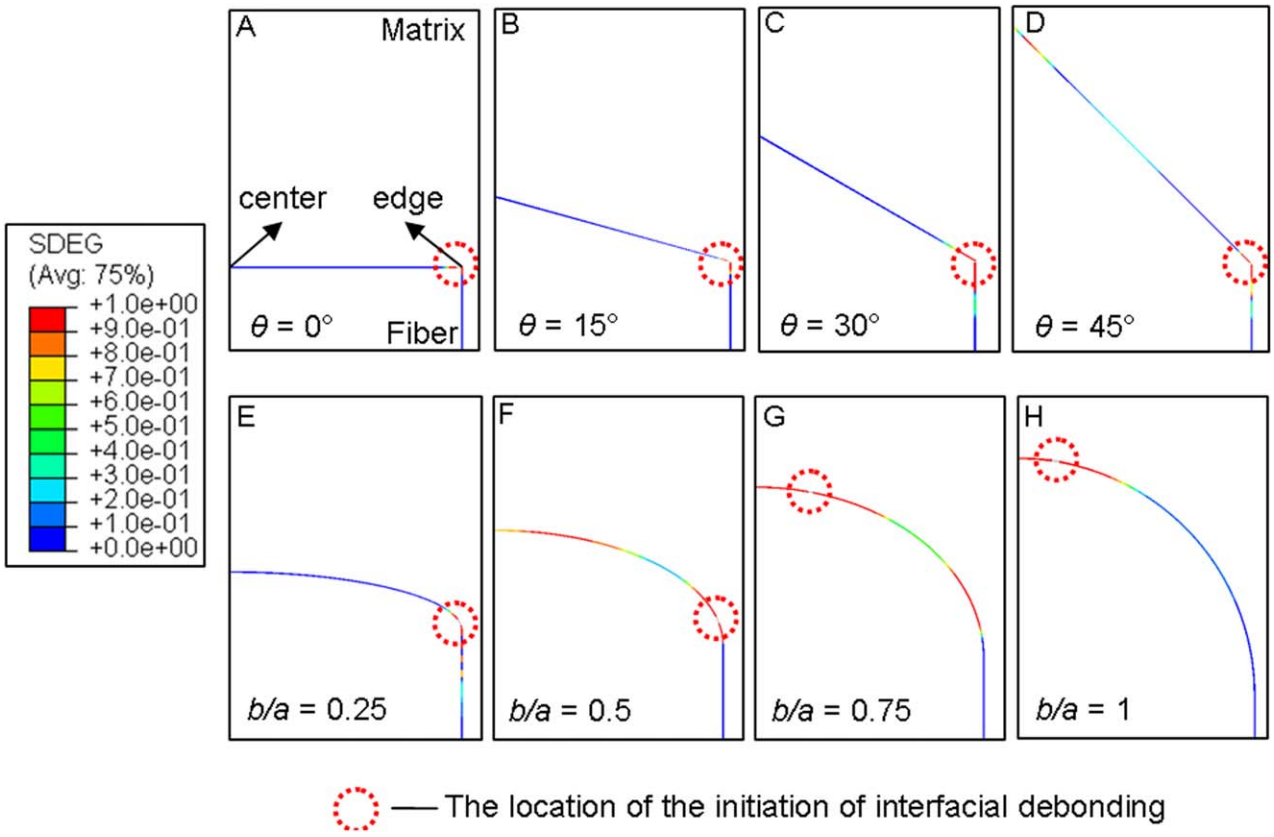

Figure 5. Initial location of the interfacial debonding with different fiber tip shapes. [Color figure can be viewed in the online issue, which is available at wileyonlinelibrary.com.]

hybrid formulation. The element chosen in this study was the linear quadrilateral hybrid element CAX4H, with a mesh sufficiently fine to provide at least two elements between each fiber. A four-node axisymmetric cohesive element, COHAX4, was introduced between each fiber and the surrounding matrix to simulate interfacial debonding. A typical model is composed of approximately 5000 elements, and the analyses carried out with finer meshes (up to 10,000 elements) provided the same results.

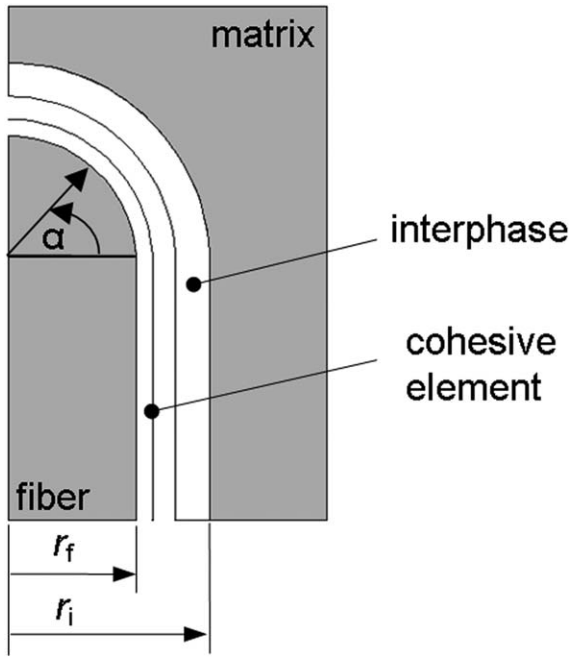

Figure 6. Individual constituents with the hemispherical fiber tip.

Properties of the Constituent Material

The aramid fiber was modeled as a linear elastic, homogeneous isotropic material. The Young's modulus of the aramid fiber (E_f) and Poisson's ratio of the aramid fiber were 136 GPa and 0.2, respectively.[25] The rubber matrix was modeled as a hyperelastic material. A neo-Hookean model was introduced, and the strain energy density function (W) for an incompressible neo-Hookean material is as follows:[27]

$$W = C_1(\bar{I}_1 - 3) \tag{2}$$

where C_1 is an empirically determined material constant and I_1 is the invariant of the deviatoric component of the left Cauchy–Green deformation tensor.

This is a convenient way to define the material model of hyperelastic composites by means of providing rubber uniaxial test data to ABAQUS. The type of the strain potential energy can then be determined according to the contrast diagrams of stress–strain curves given in ABAQUS. A neo-Hookean model is used in this article. The computed C_1 was 1.466 MPa.

Cohesive Zone Model

The cohesive zone model used to describe the damage of the interface is shown in Figure 2(c). The mechanical behavior

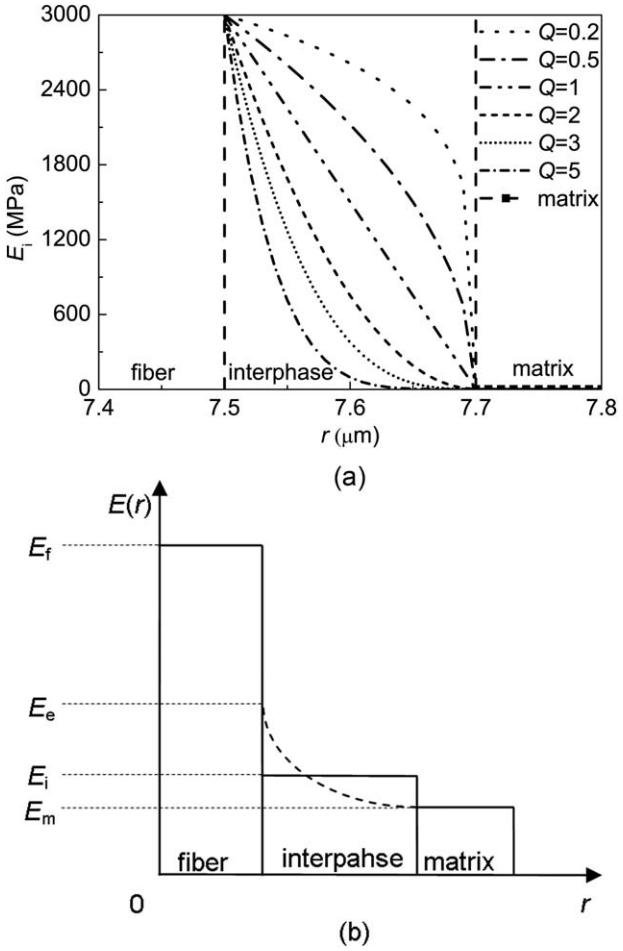

Figure 7. Modulus distribution (E(r)) along the direction of the fiber radius (r) in the three-phase model containing (a) gradient interphase and (b) equivalent interphase.

of these elements is expressed in terms of a traction–separation law, which relates the displacement jump across the interface with the traction vector acting upon it. An element size of nearly $0.03r_f$ is used in the vicinity of the interface.[28] The initial response is linear in the absence of damage, and therefore, the traction–separation law can be written as follows:

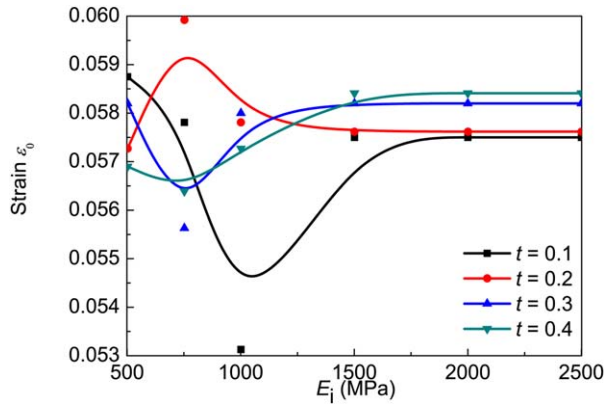

Figure 8. ε_0 values of the hemispherical fiber tip. [Color figure can be viewed in the online issue, which is available at wileyonlinelibrary.com.]

$$t_n = k\delta_n \text{ and } t_s = k\delta_s \quad (3)$$

where t_n, t_s, δ_n, and δ_s are the normal and tangential tractions and displacement jumps across the interface, respectively. An elastic stiffness (K) of 10^8 GPa/m is selected for the interface; this is large enough to ensure the displacement continuity at the interface and to prevent any modification of the stress field around the fibers in the absence of damage.[3]

Damage is assumed to be initiated when the maximum nominal stress ratio reaches one of the values given by the following equation:

$$\text{Max}\left\{\frac{\langle t_n\rangle}{t_n^0}, \frac{t_s}{t_s^0}\right\} = 1 \quad (4)$$

where the angle brackets are Macaulay brackets, which return the argument if positive and zero; otherwise, they impede the development of damage when the interface is under compression. t_n^0 and t_s^0 are the normal and shear interfacial strengths, respectively, which were assumed to be equal for simplicity (i.e., $t_n^0 = t_s^0$). δ_n^0 and δ_s^0 stand for the corresponding normal and shear displacements. Once the damage begins, the traction stress is reduced; this depends on the interfacial damage parameter (D), which evolves from 0 (in the absence of damage) to 1 (at ultimate failure), as shown in Figure 3. The normal and shear displacement at failure (δ_n^f and δ_s^f, respectively) are determined by the normal and shear fracture energy (G_n and G_s, respectively) which corresponds to the area under the traction–separation curve.

The value of the interfacial parameters were taken from refs. 3 and 26 as follows: $K = 10^8$ GPa/m, $t_n^0 = t_s^0 = 2.1$ MPa, and $G_n = G_s = 0.1$ J/m^2.

RESULTS AND DISCUSSION

Effect of the Shapes of the Fiber Tip on the Interfacial Debonding

The effects of the flat ($\theta = 0°$) and conoid ($\theta = 15$, 30, and 45°) fiber tips on the initiation of the interfacial debonding are shown in Figure 4(a). ε_0 increased as the angle of the fiber tip increased. ε_0 had a minimum 0.018 for the flat fiber tip ($\theta = 0°$), and it reached a maximum (0.035) for the conoid fiber tip ($\theta = 45°$). Therefore, the conoid fiber tip was beneficial to the restraint of the initiation of the interfacial debonding.

The effects of the hemispherical ($b/a = 1$) and semi-elliptical ($b/a = 0.25$, 0.5, and 0.75) fiber tips on the initiation of the interfacial debonding are shown in Figure 4(b). The results show that ε_0 increased as b/a increased. When the value of b/a was larger than 0.75, ε_0 varied slowly. We also found that the value of ε_0 with the hemispherical fiber tip was larger than that with the flat and conoid fiber tips. It was, therefore, clear that the hemispherical fiber tip appeared to encourage optimum behavior among all of the shapes of fiber tips.

Figure 5 shows the initial location of the interfacial debonding with different fiber tip shapes. Figure 5(A–H) corresponds to points A–H shown in Figure 4. Figure 5(A–D) shows that the initial location of the interfacial debonding remains unchanged with the increase of θ from 0 to 45°, and the debonding is initiated at the edge of the fiber tip, where the stress concentration

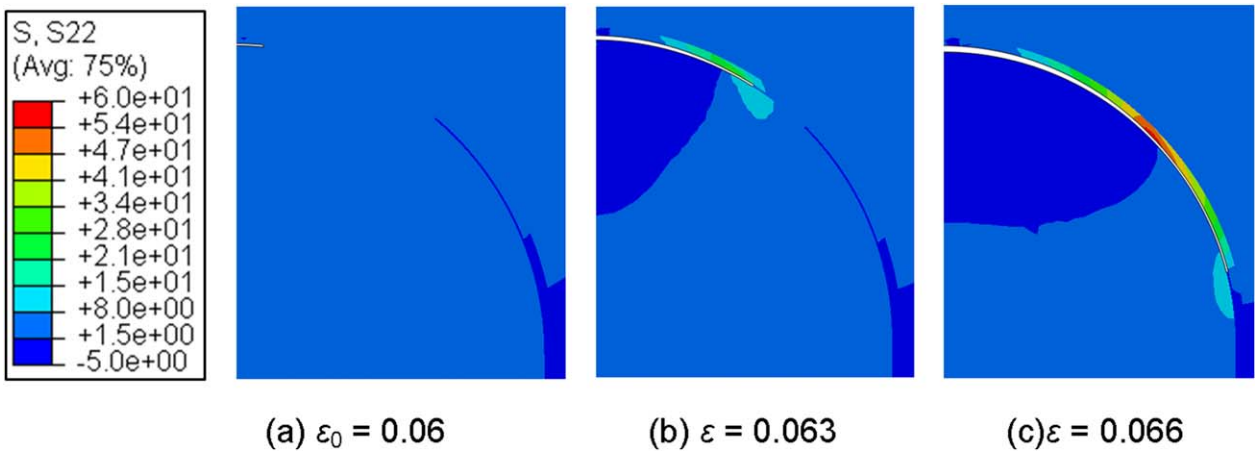

Figure 9. Evolution of interfacial debonding with the hemispherical fiber tip. (S stand for the abbreviation of the stress, and S22 are the stress along the direction of x [Color figure can be viewed in the online issue, which is available at wileyonlinelibrary.com.].

occurs. Figure 5(E–H) show that the initial locations of the interfacial debonding moved from the edge to the center of the fiber tip when b/a gradually increased. The initial locations of the interfacial debonding with the hemispherical ($b/a = 1$) and semi-elliptical fiber tips ($b/a = 0.75$) were near the center of the fiber tips; this was the reason of a larger value of ε_0.

Effect of the Interphase Properties on Interfacial Debonding

The FEM with the interphase of the hemispherical fiber tip ($b/a = 1$) was chosen for the following analysis. Figure 6 shows the established model, which incorporated the fiber, interphase, rubber matrix, and cohesive element r_i is the radius of the interphase.

The interphase property variation with radius is given by[21–24]

$$\frac{P_i(r)}{P_m} = 1 - D\left[\frac{r_i - r}{r_i - r_f}\right]^Q \quad (5)$$

where $P_i(r)$ is an interphase property, such as the elastic modulus, shear modulus, or Poisson's ratio; P_m is the resin matrix property; r is the radius; the subscripts i and f refer to the interphase and fiber, respectively; and D and Q are material parameters. D is also called an adhesion factor:

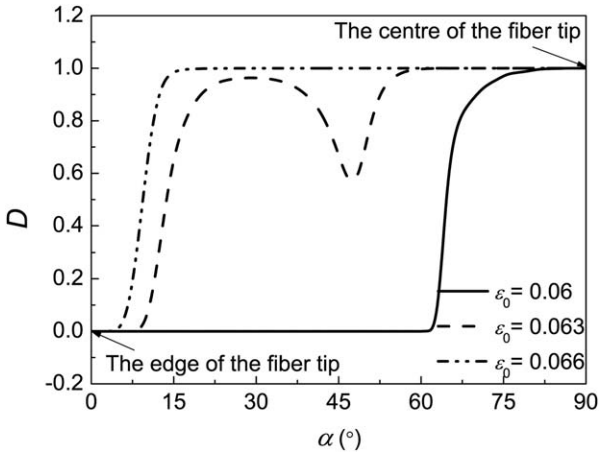

Figure 10. Distribution of D.

$$D = \left[P_m - P_i(r_f)\right]/P_m$$

To simplify the problem, the average of the gradient distribution of the interphase properties was taken as the material parameter. The average interphase properties (P_i) is given by

$$P_i = \frac{1}{(r_i - r_f)}\int_{r_f}^{r_i} P_i(r)dr \quad (6)$$

The interfacial adhesion is usually poor between the aramid fiber and rubber matrix; this restricts the mechanical properties of the composites. The reason was that the surface of the aramid fiber was smooth, there was a lack of polar groups and chemical activity. In generally, epoxy resin coating was used as the surface treatment method of the aramid fiber.[29–33] Thus, the elastic modulus of the interphase varied between $E_e = 3$ GPa (fiber coated with the epoxy resin) and $E_m = 2$ MPa (rubber matrix). The modulus distribution(E(r)) along the direction of the fiber radius (r) are shown in Figure 7(a,b), respectively.[21] In this study, the calculated average moduli of the interphase (E_i) were 502, 752, 1000, 1501, 2000, and 2500 MPa.

To investigate the influence of the interphase properties on the interfacial debonding of SFRCs with different E_i's and thicknesses (ts), the numerical analysis of an FEM with a hemispherical fiber tip were conducted. Figure 8 illustrates the relationships among ε_0, E_i, and t. The t values were regarded as 0.1, 0.2, 0.3, and 0.4 μm.[21] The results show that ε_0 varied with E_i and t, and it reached to a maximum value when t was 0.2 μm and E_i was 752 MPa. However, for the other t values, ε_0 had a relatively small value when E_i was 752 MPa. When t was 0.1 μm and E_i was 1000 MPa, ε_0 reached a minimum value. We also observed that ε_0 remained nearly unchanged when E_i was larger than 1500 MPa. Therefore, to restrain the initiation of the interfacial debonding of the SFRCs, a t of about 0.2 μm and an E_i of about 752 MPa were desired.

Figure 9 shows that the evolution of the interfacial debonding when t was 0.2 μm and E_i was 752 MPa. We observed that the interfacial debonding locations moved from the center to the

edge of the fiber tip. Figure 10 illustrates the evolution of D with the polar angle (α). The interphase element's behavior was governed by the value of D. The process of the interfacial debonding began at one point of the interface when D was greater than 0 and was complete when D was 1. The stress concentration began at a single point of the interphase when α was 90°, and after that, it developed symmetrically in a circumferential direction. For the applied ε of 0.066, the debonding was complete in the domain of $\alpha = 15$–90°, and the initial elastic region was in the domain of $\alpha = 0$–3.6°. The results from Figure 10 indicate that the debonding area grew rapidly when the applied ε_0 was 0.06 or greater.

CONCLUSIONS

In this article, an axisymmetric FEM under axial tensile load was established, where the cohesive zone model was embedded in the fiber–matrix interface. The effects of the fiber tip shapes and interphase properties on the interfacial debonding of SFRCs were investigated.

ε_0 of the SFRC reinforced with the hemispherical tip fiber appeared to be the maximum among those of the researched fiber tips. It was, therefore, clear that the hemispherical fiber tip appeared to demonstrate optimum behavior. The initial location of the interfacial debonding occurred near the center of the fiber tips with hemispherical ($b/a = 1$) and semi-elliptical fiber tips ($b/a = 0.75$), and it appeared at the edge of the fiber tips with flat, conoid, semi-elliptical fiber tips ($b/a = 0.25$ and 0.5).

ε_0 varied with E_i and t, and it reached a maximum value when t was 0.2 μm and E_i was 752 MPa. However, for the other t values, ε_0 had a relatively small value when E_i was 752 MPa. When t was 0.1 μm and E_i was 1000 MPa, ε_0 reached a minimum value. To restrain the initiation of the interfacial debonding of the SFRCs, a t of about 0.2 μm and an E_i of about 752 MPa were desired.

The initiation and evolution of the interfacial debonding at $t = 0.2$ μm and $E_i = 752$ MPa were investigated. D changed with α. The interphase element's behavior was governed by the value of D. The process of the interfacial debonding began at one point of the interface when D was greater than 0 and was completed when D was 1. The results show that the initial debonding began at a single point of the interphase for $\alpha = 90°$ and grew rapidly when ε_0 was 0.06 or greater.

The results presented in this article indicate that the performances of the SFRCs depended significantly on the fiber tip shapes and the interphase properties, and they could be improved by the proper modulation of the fiber tip and the design of the appropriate E_i and t values.

ACKNOWLEDGMENTS

This project was supported by the National Natural Science Foundation of China (contract grant number 51375223) and by Jiangsu Province ordinary university graduate research and innovation (contract grant number CXZZ11_0337).

REFERENCES

1. Gu, B. Q.; Chen, Y.; Zhou, J. F. Advances in Composite Materials—Ecodesign and Analysis; Brahim, A., Ed.; InTech: Rijeka, Croatia, **2011**.
2. Zhu, D. S.; Gu, B. Q.; Chen, Y. *J. Comput. Theory Nanosci.* **2008**, *5*, 1546.
3. Zhang, B.; Gu, B.; Yu, X. *J. Appl. Polym. Sci.* **2015**, *132*. DOI: 10.1002/app.41672.
4. Vaughan, T. J.; McCarthy, C. T. *Compos. Sci. Technol.* **2011**, *71*, 388.
5. Hobbiebrunken, T.; Hojo, M.; Adachi, T.; De Jong, C.; Fiedler, B. *Compos. A* **2006**, *37*, 2248.
6. Canal, L. P.; González, C.; Segurado, J.; Llorca, J. *Compos. Sci. Technol.* **2012**, *72*, 1223.
7. Kim, H. G. *Mater. Sci. Eng. A* **2008**, *483*, 135.
8. Starink, M. J.; Syngellakis, S. *Mater. Sci. Eng. A* **1999**, *270*, 270.
9. Moraleda, J.; Segurado, J.; Llorca, J. *J. Mech. Phys. Solids* **2009**, *57*, 1596.
10. Li, X.; Xia, Y.; Li, Z.; Xia, Y. *Comput. Mater. Sci.* **2012**, *55*, 157.
11. Nishikawa, M.; Okabe, T.; Takeda, N. *Mater. Sci. Eng. A* **2008**, *480*, 549.
12. Nishikawa, M.; Okabe, T.; Hemmi, K.; Takeda, N. *Int. J. Solids Struct.* **2008**, *45*, 4098.
13. Afonso, J. C.; Ranalli, G. *Compos. Sci. Technol.* **2005**, *65*, 1264.
14. Wang, X.; Zhao, W.; Fang, B.; Lu, S.; Zhang, Y. *J. Appl. Polym. Sci.* **2015**, *132*. DOI: 10.1002/app.41573.
15. Huo, S.; Chevali, V. S.; Ulven, C. A. *J. Appl. Polym. Sci.* **2013**, *128*, 3490.
16. Zhang, B.; Gu, B. Q. In Applied Mechanics and Materials Revealed: Proceedings of 2011 International Conference on Recent Trends in Materials and Mechanical Engineering, Shenzhen, China, Jan 27–28, 2001; Trans Tech: Bremen, Germany, 2011; pp 55, 303.
17. Yuan, M. N.; Yang, Y. Q.; Huang, B.; Wu, Y. *J. Rare Met. Mater. Eng.* **2009**, *38*, 1321.
18. Reifsnider, K. L. *Composites* **1994**, *25*, 461.
19. Papanicolaou, G. C.; Anifantis, N. K.; Keppas, L. K.; Kosmidou, T. V. *Compos. Interfaces* **2007**, *14*, 131.
20. Kim, J. K.; Sham, M. L.; Wu,J. *Compos. A* **2001**, *32*, 607.
21. Shen, L.; Li, J. *Int. J. Solids Struct.* **2003**, *40*, 1393.
22. Kiritsi, C. C.; Anifantis, N. K. *Comput. Mater. Sci.* **2001**, *20*, 86.
23. Ngabonziza, Y.; Li, J.; Barry, C. F. *Acta Mech.* **2011**, *220*, 289.
24. Sevostianov, I.; Rodriguez-Ramos, R.; Guinovart-Diaz, R.; Bravo-Castillero, J.; Sabina, F. J. *Int. J. Solids Struct.* **2012**, *49*, 1518.
25. Yu, X.; Gu, B.; Zhang, B. *J. Appl. Polym. Sci.* **2015**, *132*. DOI: 10.1002/app.41638.
26. Sa, R.; Yan, Y.; Wei, Z.; Zhang, L.; Wang, W.; Tian, M. *ACS Appl. Mater. Interface* **2014**, *6*, 21730.

27. Jiménez, F. L.; Pellegrino, S. *Int. J. Solids Struct.* **2012**, *49*, 635.
28. Romanowicz, M. *Comput. Mater. Sci.* **2009**, *47*, 225.
29. Gao, Z.; Ma, D.; Lv, X.; Zhang, Y. *J. Appl. Polym. Sci.* **2013**, *128*, 1036.
30. Chattopadhyay, S. K.; Khandal, R. K.; Uppaluri, R.; Ghoshal, A. K. *J. Appl. Polym. Sci.* **2011**, *119*, 1619.
31. Zhang, X.; Chen, P.; Han, D.; Yu, Q.; Ding, Z.; Zhu, X. *Appl. Surf. Sci.* **2013**, *266*, 110.
32. Shirazi, M.; Talma, A. G.; Noordermeer, J. W. M. *J. Appl. Polym. Sci.* **2013**, *128*, 2255.
33. Chen, X.; Zhang, S.; Xu, G.; Zhu, X.; Liu, W. *J. Appl. Polym. Sci.* **2012**, *125*, 1166.